processes

MDPI

Article

Research and Application of a Visual Simulation and Evaluation Apparatus for the Fracture Plugging Process

Yan Ye [1,*], Xingyu Li [1,*], Fuliang Guo [2], Ning Yang [1], Feng Lu [1], Yayun Guo [1] and Shucheng Dai [1]

[1] State Key Laboratory of Petroleum Resources and Engineering, College of Petroleum Engineering, China University of Petroleum, Beijing 102249, China
[2] Tarim Oilfield Company, Korla 841000, China
* Correspondence: yeyan@cup.edu.cn (Y.Y.); lxypetroleum@163.com (X.L.)

Abstract

Lost circulation in fractured formations is a major challenge during drilling operations, while conventional plugging evaluation methods relying solely on pressure-bearing curves and fluid-loss data often fail to accurately distinguish effective internal plugging from ineffective plugging behavior. To address this issue, a visualized plugging evaluation apparatus with high pressure-bearing capacity and large-window observation capability was developed to directly observe the plugging process and evaluate plugging performance under different fracture conditions. Based on the Ideal Packing Theory and the D_{90} rule, plugging formulations were systematically evaluated under different fracture-width coefficients, slurry concentrations, and fracture-width conditions. The results showed that excessively large fracture-width coefficients or excessively high slurry concentrations could lead to premature "external plugging," in which plugging materials accumulated near the fracture entrance without forming effective internal plugging structures. Although such cases exhibited rapid pressure buildup, visual observations confirmed that the fracture itself remained insufficiently sealed. Under the present experimental conditions, the optimized formulation with a fracture-width coefficient of 0.8 W and a slurry concentration of 25% exhibited the best overall plugging performance. The formulation reached 10 MPa in approximately 2650 s and successfully formed stable internal plugging structures under different fracture-width conditions, with the maximum variation in plugging time remaining within 7%. Field applications in Well BD-X further validated the effectiveness of the proposed method and optimized formulations under real drilling conditions. The developed apparatus and evaluation method provide a reliable experimental approach for optimizing plugging formulations and preventing lost circulation in fractured formations.

Keywords: fractured lost circulation; plugging apparatus; visualization; plugging evaluation; external plugging

Check for updates

Academic Editor: Federica Raganati

Received: 30 October 2025
Revised: 25 May 2026
Accepted: 28 May 2026
Published: 23 June 2026

Copyright: © 2026 by the authors. Licensee MDPI, Basel, Switzerland. This article is an open access article distributed under the terms and conditions of the Creative Commons Attribution (CC BY) license.

1. Introduction

Lost circulation in fractured formations is one of the most frequent and severe downhole incidents encountered during drilling operations [1,2]. It not only consumes large volumes of drilling fluid and prolongs the drilling cycle, but may also induce wellbore collapse, blowout, pipe sticking, and even well abandonment if not properly controlled [1–3]. With oil and gas exploration extending toward deep, ultra-deep, unconventional, and low-grade reservoirs, fractured and fractured-vuggy formations have

become increasingly common drilling targets, making lost circulation control more challenging. Statistical data further highlight the severity of this problem. Lost circulation occurs in approximately 20–25% of drilled wells worldwide, and the annual cost associated with lost-circulation control has been reported to reach approximately USD 4 billion. In North American carbonate and shale reservoirs, severe lost circulation occurs in approximately 40% of drilled wells, whereas in Middle Eastern fractured carbonate reservoirs, the proportion exceeds 30%, with lost-circulation-related non-productive time accounting for more than 50% [3]. In the Kuqa piedmont area of the Tarim Basin, 354 lost-circulation events occurred in 76 completed wells from 2017 to 2019, among which severe lost circulation accounted for 65% [3]. Therefore, improving the understanding of plugging behavior and developing reliable evaluation methods are of great importance for fractured lost-circulation control.

To address lost circulation, research has evolved from empirical field treatment toward mechanism-based design, laboratory simulation, and quantitative evaluation. Early lost-circulation control mainly relied on field experience and conventional bridging materials. Subsequently, wellbore-strengthening theories and plugging mechanisms were developed to improve the scientific basis of lost-circulation control. Representative concepts include stress cage theory, plugged-zone theory, and strength-ring theory, which aim to enhance formation pressure-bearing capacity by regulating stress distribution, forming low-permeability plugging zones, or constructing high-strength sealing structures around the wellbore [1]. In parallel, different types of lost circulation materials, including bridging materials, high-filtration-loss materials, swelling materials, flexible gels, curable materials, and intelligent materials, have been developed for different types of lost formations [3]. These developments have improved plugging performance in porous and small-fracture formations. However, for large fractured and fractured-vuggy formations, plugging performance remains unstable because of poor material retention, insufficient filling, weak matching between material particle size and fracture scale, and the frequent occurrence of premature plugging near the fracture inlet.

Laboratory plugging simulation apparatuses provide an essential platform for evaluating LCM formulations, optimizing plugging techniques, and investigating plugging mechanisms [4,5]. The development of these apparatuses has generally followed a progressive route from static slot-based evaluation, to high-temperature/high-pressure simulation, to dynamic and stress-sensitive fracture modeling, and finally to rough-fracture and visualized experimental systems. The API plugging test apparatus is one of the earliest and most widely used laboratory instruments for evaluating plugging treatments. It simulates fractures using a slotted copper disk and provides a simple and repeatable method for comparing plugging materials. However, its limited operating pressure and ambient-temperature conditions cannot meet the requirements for pressure-bearing simulations in deep and ultra-deep wells [6]. To improve downhole condition simulation, high-pressure and HTHP plugging apparatuses were subsequently developed. For example, Hettema et al. [7] designed a high-pressure fracture plugging tester in 2007, and Deng [8] developed an HTHP plugging simulation apparatus in 2012. These devices improved the simulation of pressure and temperature conditions, but most still relied on simplified static fracture geometries and lacked direct observation of the plugging process.

As research progressed, more attention was paid to fracture deformation, stress sensitivity, and flow conditions during plugging. Dou et al. [9] developed a high-fidelity plugging evaluation device in 2009, while Hou et al. [10] proposed a stress-sensitive formation plugging simulation device in 2010 by incorporating a confining pressure chamber. Peng et al. [11] further developed a device capable of simulating dynamically varying fracture widths, and Jiang et al. [12] designed an apparatus for simulating annular-flow

plugging conditions. More recently, Ma et al. [13] improved dynamic fracture plugging evaluation by incorporating reverse pressure-bearing tests. These systems enhanced the capability to simulate fracture deformation and dynamic plugging behavior, but their evaluation still mainly depended on terminal parameters such as pressure-bearing capacity and fluid loss.

Another important development direction has been the reconstruction of fracture surface morphology. Zhao et al. [14] simulated rough fracture walls by attaching sandpaper to the fracture module, and Pu et al. [15] modified the API fracture module by increasing fracture length and roughness. Hou et al. [16] designed a true triaxial drilling plugging simulation apparatus using artificial fractured cores under in situ stress conditions. Wang et al. [17] further introduced 3D scanning and printing technology to fabricate simulated fracture models with more realistic fracture characteristics. These approaches improved the representation of natural fracture morphology and stress conditions. Nevertheless, most of these systems still could not directly visualize LCM transport, retention, and plug evolution within the fracture.

To overcome the limitation of non-visual evaluation, visualized plugging simulation systems have been increasingly developed. Shi et al. [18] used laser-etched tempered glass to construct micron-scale fractures and study visual plugging behavior in shale microfractures. Huang et al. [19] investigated proppant transport and retention in rough vertical fractures using a semi-transparent fracture model. Li [20] developed a gas–liquid displacement and gas invasion prevention test apparatus using steel wedge plates and smooth transparent plexiglass plates, but the apparatus suffered from limited transparency and low pressure-bearing capacity. Xu et al. [21] investigated microscopic plugging mechanisms using a borosilicate-glass visual apparatus, and Guo et al. [22] studied temporary plugging particle behavior in hydraulic fractures, proposing two stages and four modes of plug formation. Although these visualized systems improved the understanding of particle transport and plug formation, their pressure-bearing capacity was generally low, with some systems reaching only approximately 1 MPa, which limits their applicability to practical high-pressure plugging evaluation.

Figure 1 summarizes the historical evolution of laboratory evaluation methods for fractured lost-circulation control. Overall, existing laboratory systems have advanced from simple static slot tests toward high-pressure, dynamic, rough-fracture, and visualized simulations. However, several limitations remain: (1) conventional non-visual apparatuses cannot directly identify the location and morphology of the plugging zone; (2) many visualized systems lack sufficient pressure-bearing capacity for deep and ultra-deep well conditions; and (3) current evaluation methods may misinterpret rapid pressure buildup caused by external plugging as effective internal plugging. Therefore, a visual apparatus that combines high pressure-bearing capacity, high visualization clarity, and reliable fracture-flow simulation is still needed.

To address these limitations, this study develops a visual experimental apparatus for observing the fracture plugging process. The apparatus integrates high visualization clarity, high pressure-bearing capacity, and real-time recording capability, enabling direct observation of LCM migration, retention, plug formation, and external plugging behavior. Based on this apparatus, plugging formulations designed using the Ideal Packing Theory and D_{90} rule are evaluated under different fracture width factors, slurry concentrations, and fracture-width profiles. The results provide a more reliable basis for optimizing LCM formulations and improving lost-circulation control in fractured formations.

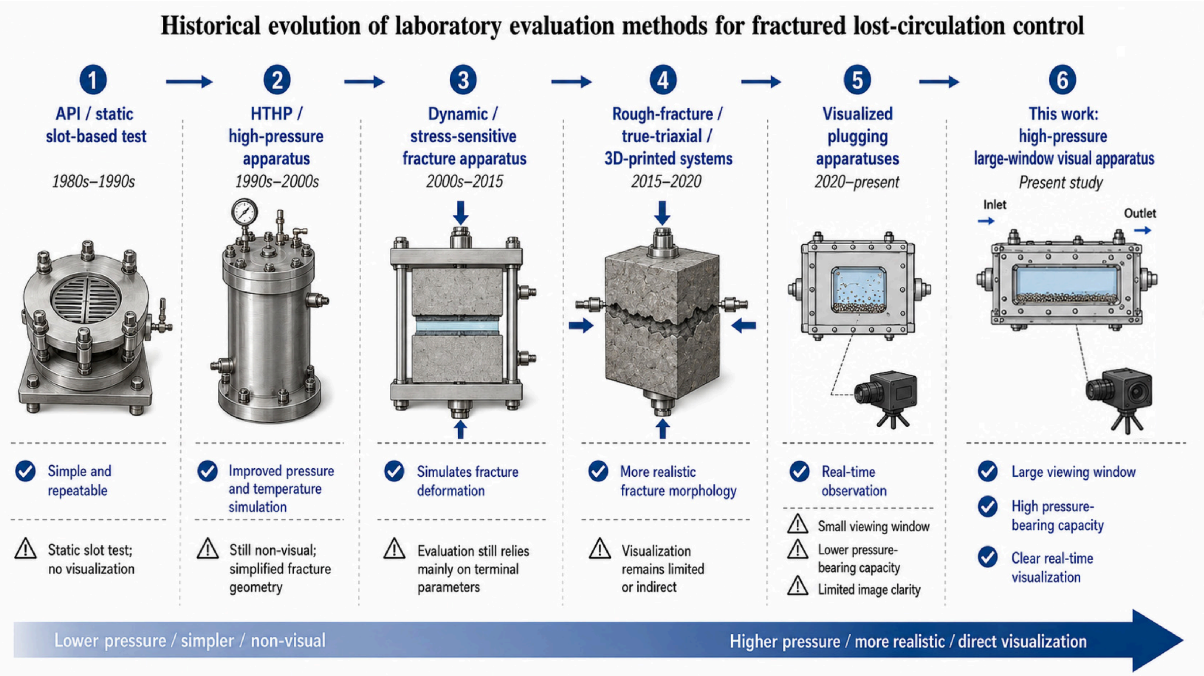


Figure 1. Historical evolution of laboratory evaluation methods for fractured lost-circulation control.

2. Visual Experimental Apparatus and Methodology

2.1. Experimental Apparatus

To address the limitations of existing plugging simulation devices for fractured formations, this study developed a visual experimental apparatus featuring three key innovations: (1) the integration of high transparency with high pressure-bearing capability, enabling direct observation of the plugging process under elevated-pressure conditions; (2) a large-window visual fracture model for tracking particle migration, retention, and plug evolution within the fracture; and (3) a specially designed wedge-shaped flow-channel structure that minimizes premature plugging at the fracture inlet and improves the reliability of plugging evaluation. The apparatus comprises five main modules: an injection system, a fluid storage system, a fracture simulation system, a data acquisition system, and a control system (Figure 2). It is capable of simulating the plugging process after drilling fluid carrying LCMs enters the fracture, thereby enabling effective evaluation of plugging formulation performance.

(1) Injection System

The fluid injection system, serving as the power core of the entire plugging apparatus, comprises an air-driven pump and a constant-rate/constant-pressure (CRCP) pump. The air-driven pump supplies the pneumatic power for the CRCP pump, while the CRCP pump directly drives the injection of the LCM slurry. This CRCP pump incorporates two injection pumps and two piston accumulators, each with a volume of 550 mL. Through an alternating operation mechanism of the dual pumps, it continuously maintains a stable injection rate and pressure, thereby ensuring operational stability throughout the entire injection process.

(2) Fluid Storage System

Positioned between the fluid injection system and the fracture simulation system, this unit integrates three primary functions: storage, agitation, and heating, as shown in Figure 3. The agitator ensures that the LCM slurry remains homogeneously suspended and prevents sedimentation prior to entering the fracture. The heating system is designed to simulate the

elevated temperature conditions of deep and ultra-deep reservoirs, facilitating the study of temperature effects on drilling fluid performance. A floating piston is incorporated within the system to effectively isolate the LCM slurry from the injection water of the pump system, preventing mutual contamination and thereby ensuring the integrity of the slurry performance.

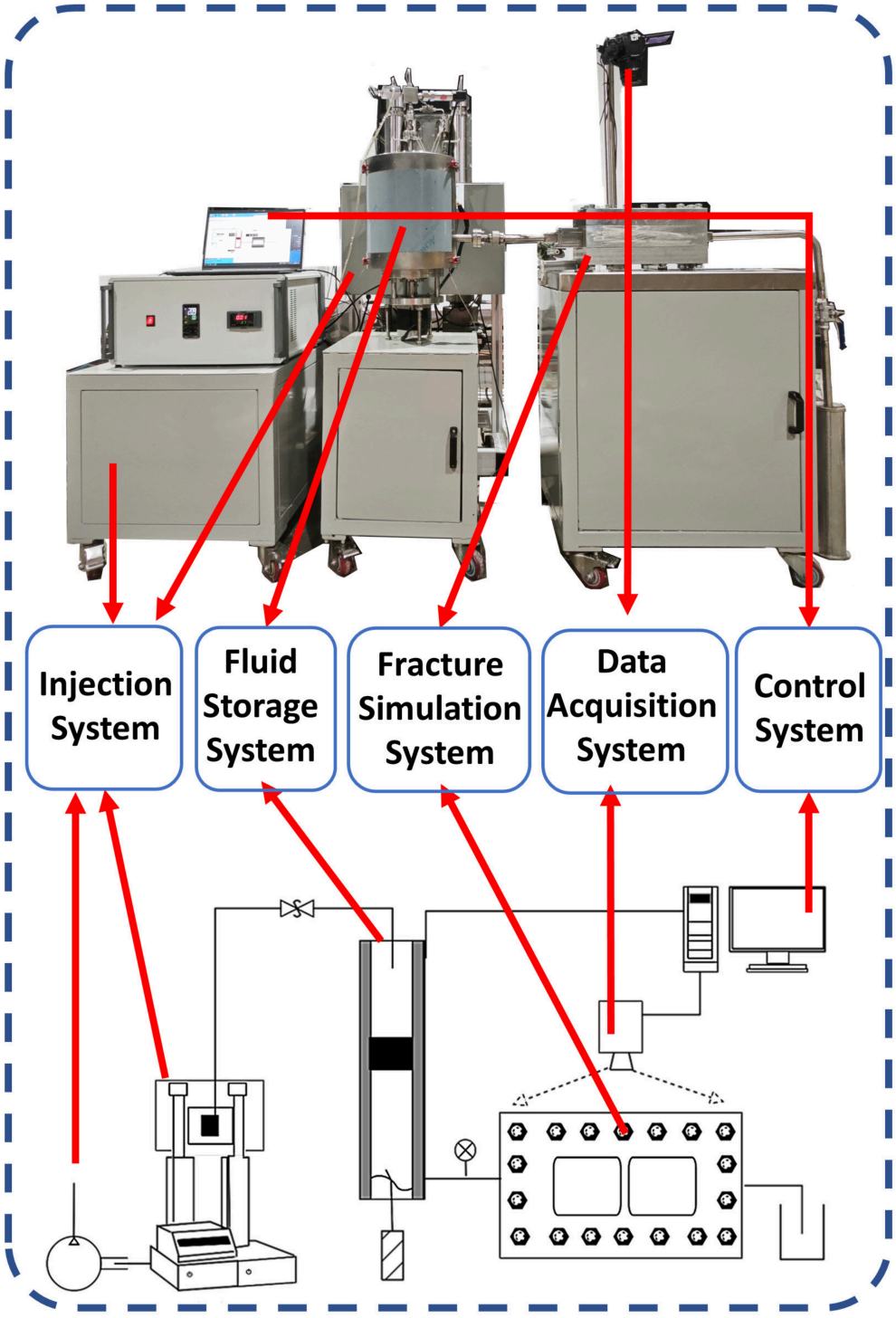


Figure 2. Schematic diagram of the visual experimental apparatus for the fracture plugging process.

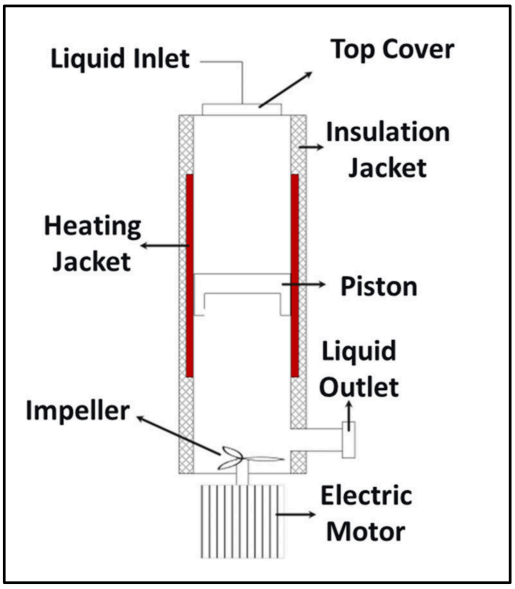


Figure 3. Schematic diagram of the fluid storage container.

(3) Fracture Simulation System

The fracture simulation system, serving as the core component of the entire visual plugging apparatus, primarily utilizes highly transparent borosilicate glass and stainless steel as its main structural materials. In the structural design, stainless steel is employed to fabricate the central frame and the upper/lower cover plates of the visual fracture model, with sealing achieved using rubber O-rings and polytetrafluoroethylene (PTFE) gaskets. The borosilicate glass is precisely embedded and secured within the grooves of the central frame. This design effectively transfers the majority of the pressure load to the stainless steel frame, thereby ensuring a high overall pressure-bearing capacity for the fracture model. To address different pressure-bearing requirements, two distinct fracture models were developed through structural modifications to the cover plates and central frame: a High-Pressure Visual Fracture Model (Figure 4a) and a Large-Window Visual Fracture Model (Figure 4b). Furthermore, a flow channel is incorporated at the fracture inlet (Figure 4d). Its function is to facilitate a smooth transition of the fluid from the inlet to the observation zone, ensuring that the fracture height within the visual window attains the designed wedge-shaped profile.

(4) Data Acquisition System

This subsystem, comprising pressure sensors, a temperature sensor, a high-definition camera, and a computer, is responsible for the real-time acquisition of system pressure and temperature data. It simultaneously records video footage of the plugging process. All data are logged and saved on the local computer for subsequent analysis.

(5) Control System

Operated via a computer and a control cabinet linked to the injection, storage, and data acquisition systems, this subsystem provides integrated control. It enables centralized start/stop commands, parameter configuration, and safety protection for all interconnected systems.

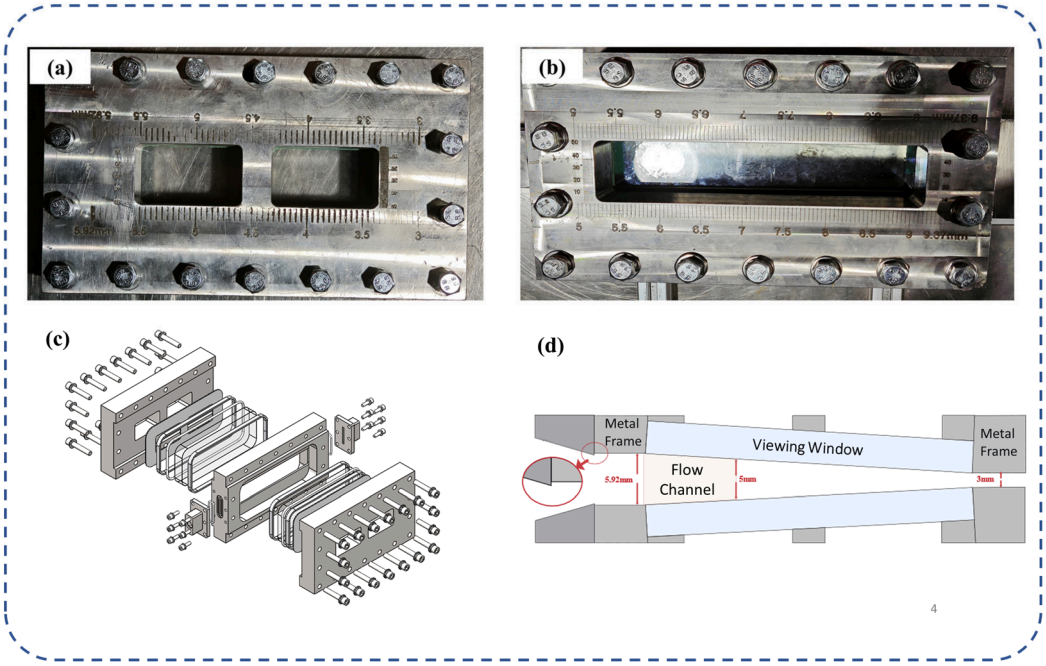


Figure 4. (**a**) High-Pressure Visual Fracture Model; (**b**) Large-window visual fracture model; (**c**) Exploded view of the fracture model; (**d**) Schematic diagram of the flow channel.

2.2. Apparatus Features

The detailed functional features corresponding to the above design innovations are described as follows. The injection system employs a Constant-Rate/Constant-Pressure (CRCP) pump with an intelligent control system, enabling a preset target pressure. Once the set pressure is reached, the pump automatically adjusts the flow rate to maintain it, allowing for a more precise assessment of the plug's pressure-bearing capacity. To accommodate various simulation requirements, six fracture models were designed, covering inlet-to-outlet height combinations of 3–1 mm, 5–3 mm, and 8–5 mm, with maximum pressure ratings of 10 MPa and 15 MPa. A critical innovation lies in the flow channel design within the fracture models, ensuring that the fracture height in the visual window strictly follows the intended wedge shape. Moreover, this design prevents premature, non-formula-related plugging at the inlet caused by abrupt flow path changes, thereby enhancing the accuracy and reliability of the experiments.

The core advantage of this apparatus is the integration of high visualization clarity with robust performance. Equipped with a high-clarity visual window, it allows direct observation of LCM transport and retention, facilitating precise determination of the final plug location and avoiding misinterpretation of ineffective external plugging.

Finally, the integrated software provides centralized control over all subsystems, enabling real-time acquisition and recording of system parameters (pressure, flow rate, temperature) and video documentation of the entire process, thus facilitating comprehensive data analysis.

2.3. Key Technical Specification

The key technical specifications of the apparatus are presented below. The injection system features a flow rate range of 0.01–120 mL/min, a stroke resolution of 0.01 mL, and a pressure range of 0–70 MPa. The fluid storage system features a capacity of 2000 mL, an agitation speed range of 0–1200 rpm, a heating range from ambient temperature to 160 °C, and a maximum pressure rating of 25 MPa. For the core fracture simulation system, the fracture length is 270 mm and the width is 50 mm, supporting inlet-to-outlet height profiles

of 3–1 mm, 5–3 mm, and 8–5 mm. Two primary model types are used: a High-Pressure Visual Fracture Model with a maximum pressure rating of 15 MPa and a visual window measuring 87.5 mm × 50 mm × 2 mm, and a Large-Window Visual Fracture Model rated for 10 MPa with a visual window measuring 50 mm × 260 mm.

2.4. Experimental Evaluation Methodology

(1) Fracture Model Installation. Select the appropriate fracture model according to the experimental plan. First, install the central frame, then mount the borosilicate glass panels on both sides of it. Subsequently, place the upper and lower cover plates and uniformly tighten the fastening bolts. Securely install the fully assembled fracture model onto the experimental platform.

(2) Equipment and Manifold Connection. Connect the components in the following sequence: air-driven pump → CRCP pump → fluid storage container → visual fracture model → waste fluid collection tank. Then, connect to the power supply. Open the air source switch and the ventilation valve. Initiate and calibrate the image acquisition system to ensure the visual window is entirely and clearly within the capture frame.

(3) LCM Slurry Preparation and Loading. Transfer the pre-prepared LCM slurry into the fluid storage container. Activate the agitation function to maintain a homogeneous suspension. Insert the floating piston, plug the top cover, and close the top drain valve.

(4) Parameter Setting and Experiment Initiation. Set the pump parameters (flow rate or pressure) as required by the experimental protocol. For a constant-flowrate test, preset the target pressure. Start the pressure, temperature, and video data acquisition systems sequentially. If slurry heating is required, activate the heating system of the storage container. Begin pressurization by starting the injection pump only after the temperature acquisition system indicates that the preset temperature has been reached. Simultaneously, open the outlet valve to collect any leaked fluid.

(5) Data Monitoring and Experiment Termination. Monitor the experimental data in real time. The experiment is considered complete when the pressure within the fracture reaches the set value and remains stable for 10 min or longer. Then, terminate the test, save all data, dismantle the setup, and clean all components.

3. Experimental Application

3.1. Experimental Materials

The plugging materials used in this experiment were JXD-series calcite materials and SQD-98 (fine) (Figure 5), which are commonly employed in the Tarim Oilfield (Korla, China); their specific parameters are listed in Table 1. A 1% concentration of xanthan gum solution (Hefei BASF Biological Technology Co., Ltd., Hefei, China; Model: H0300) was selected as the transparent base plugging slurry for the experiments. This composition ensured visual clarity while maintaining adequate particle suspension and slurry mobility.

Table 1. Parameters of Experimental Lost Circulation Materials.

Category	Composition	Model Number	Size Range (Mesh)	Morphology
JXD series	granular calcite	JXD-1	50–100	Powder form
		JXD-2	30–60	granulated
		JXD-3	18–50	granulated
		JXD-4	10–30	granulated
		JXD-4^{+}	5–14	granulated
		JXD-C	3–6	granulated
SQD-98 series	-	SQD-98 (Fine)	-	Powder form

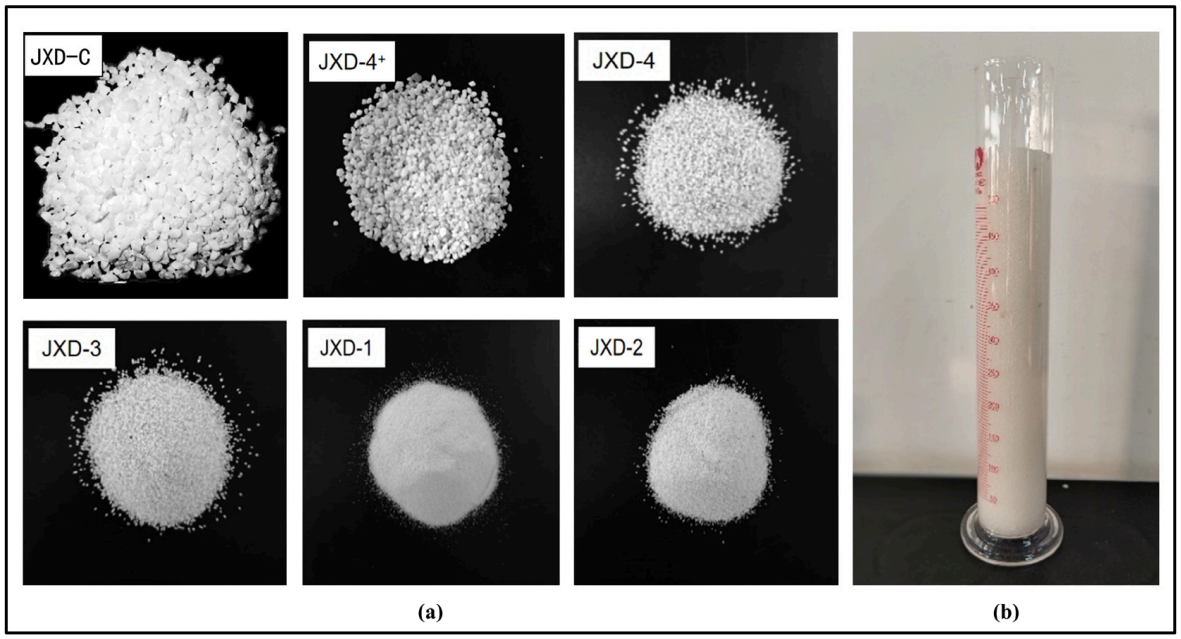


Figure 5. (**a**) JXD-series calcite lost-circulation materials (JXD-C, JXD-4^{+}, JXD-4, JXD-3, JXD-1, and JXD-2); (**b**) 1% xanthan-gum-based transparent plugging slurry.

3.2. Experimental Design

For plugging materials targeting a 5 mm fracture width, the formulations in this study were designed using BridgePRO, a software independently developed by CNPC. The design is based on the Ideal Packing Theory and the D_{90} rule, both of which have been widely used for optimizing the particle size distribution of bridging agents in drilling fluids and lost-circulation materials. The Ideal Packing Theory was developed from the principle of maximum particle packing efficiency, and the D_{90} rule provides a practical criterion for selecting the characteristic particle size of bridging materials according to the target pore or fracture size [23,24].

According to the Ideal Packing Theory, the packing efficiency of a particle system is maximized and the resulting plug layer is densest with optimal bridging performance when the cumulative volume fraction of particles exhibits a linear relationship with the square root of particle size ($d^{1/2}$). The D_{90} rule is a practical implementation of this theory: when the D_{90} value of the particle size distribution (i.e., the particle size below which 90% of the particles lie) is properly matched with the fracture aperture, an effective bridging and sealing structure can be formed.

Recent studies have further shown that the D_{90}-to-aperture relationship and the particle size distribution (PSD) of lost circulation materials significantly influence particle entry, bridging location, and sealing stability in fractures [25,26]. Yang et al. also used CT scanning and three-dimensional visualization to analyze the internal structure and particle distribution of fracture sealing bodies, demonstrating the applicability of D_{90}-based PSD design in evaluating particle accumulation and bridging behavior within fractures [27].

In this approach, a fracture width factor (W) is introduced as a dimensionless parameter to relate the D_{90} value to the fracture width:

$$D_{90} = W \times Fracture\ Width$$

where D_{90} is the particle size below which 90% of the plugging material particles lie in the cumulative size distribution; W is the fracture width factor, a dimensionless parameter used to adjust the relative size of particles to the fracture; Based on the D_{90} rule, formu-

lations corresponding to different W values (0.6 W, 0.7 W, 0.8 W, 0.9 W, and 1.0 W) were designed (specific formulations are listed in Table 2), and their plugging performance was subsequently tested and compared during the experimental phase.

Table 2. LCM Formulations Designed Based on the D_{90} Rule for a 5 mm Fracture Width.

NO.	Fracture Width Coefficient	Formulation
Formulation 1	1.0 W	5.27%JXD-C + 5.21%JXD-4$^+$ + 1.47%JXD-4 + 1.31%JXD-3 + 0.77%JXD-2 + 1.79%JXD-1 + 4.17%SQD-98 (Fine)
Formulation 2	0.9 W	4.47%JXD-C + 5.49%JXD-4$^+$ + 1.55%JXD-4 + 1.39%JXD-3 + 0.81%JXD-2 + 1.89%JXD-1 + 4.41%SQD-98 (Fine)
Formulation 3	0.8 W	3.53%JXD-C + 5.82%JXD-4$^+$ + 1.65%JXD-4 + 1.47%JXD-3 + 0.86%JXD-2 + 2%JXD-1 + 4.67%SQD-98 (Fine)
Formulation 4	0.7 W	2.39%JXD-C + 6.23%JXD-4$^+$ + 1.76%JXD-4 + 1.57%JXD-3 + 0.91%JXD-2 + 2.14%JXD-1 + 5.00%SQD-98 (Fine)
Formulation 5	0.6 W	7.70%JXD-4$^+$ + 1.90%JXD-4 + 1.70%JXD-3 + 0.99%JXD-2 + 2.31%JXD-1 + 5.40%SQD-98 (Fine)

To further clarify the experimental arrangement, the plugging tests were organized into three sequential series. First, the fracture width factor was screened using the formulations listed in Table 2 under a fixed slurry concentration. Then, the influence of slurry concentration was evaluated based on the W value selected from the fracture width factor tests. Finally, the applicability of the selected formulation was examined using fracture models with different width profiles. The main operating conditions and replicate arrangement for these three experimental series are summarized in Table 3.

Table 3. Test matrix and replicate arrangement for the plugging evaluation experiments.

Experimental Series	Fracture Model	W Value	Slurry Concentration/%	Target Pressure/MPa	Temperature Set-Point	Pump Mode	Number of Trials, *n*
Fracture width factor test	5–3 mm	0.6, 0.7, 0.8, 0.9, 1.0	20	10	Ambient temperature	Constant-rate injection with target-pressure control	3
Formulation concentration test	5–3 mm	Determined from the fracture width factor test	10, 15, 20, 25, 30	10			
Adaptability test for different fracture-width profiles	3–1 mm 5–3 mm 8–5 mm		Determined from the formulation concentration test	15			

3.3. Results and Discussion

3.3.1. Plug Formation Process

Using the visual plugging apparatus, the plugging process under various conditions was observed and can be divided into three stages, as shown in Figure 6: (a) initial bridge

formation, (b) fragmentation and reorganization of the plug, and (c) formation of a stable plug. Initially, the drilling fluid carries a substantial amount of plugging materials into the fracture. The plugging material (LCM) particles are subsequently retained at different locations within the fracture depending on the relationship between their particle size and the fracture width. Particles that are too large struggle to enter the fracture, whereas overly fine particles are easily carried out of the fracture exit. As particles continue to accumulate within the fracture, they gradually form an initial bridge structure (Figure 6a). Subsequent particles continuously deposit on this bridge, resulting in a corresponding increase in pressure. When the pressure reaches the current bearing limit of the structure, the plug undergoes fragmentation and reorganization, causing an instantaneous drop in pressure. Pressure rises again as a new plug structure forms. This cycle of fragmentation and reorganization may occur multiple times during the plug formation process until a stable plug is ultimately established (Figure 6c).

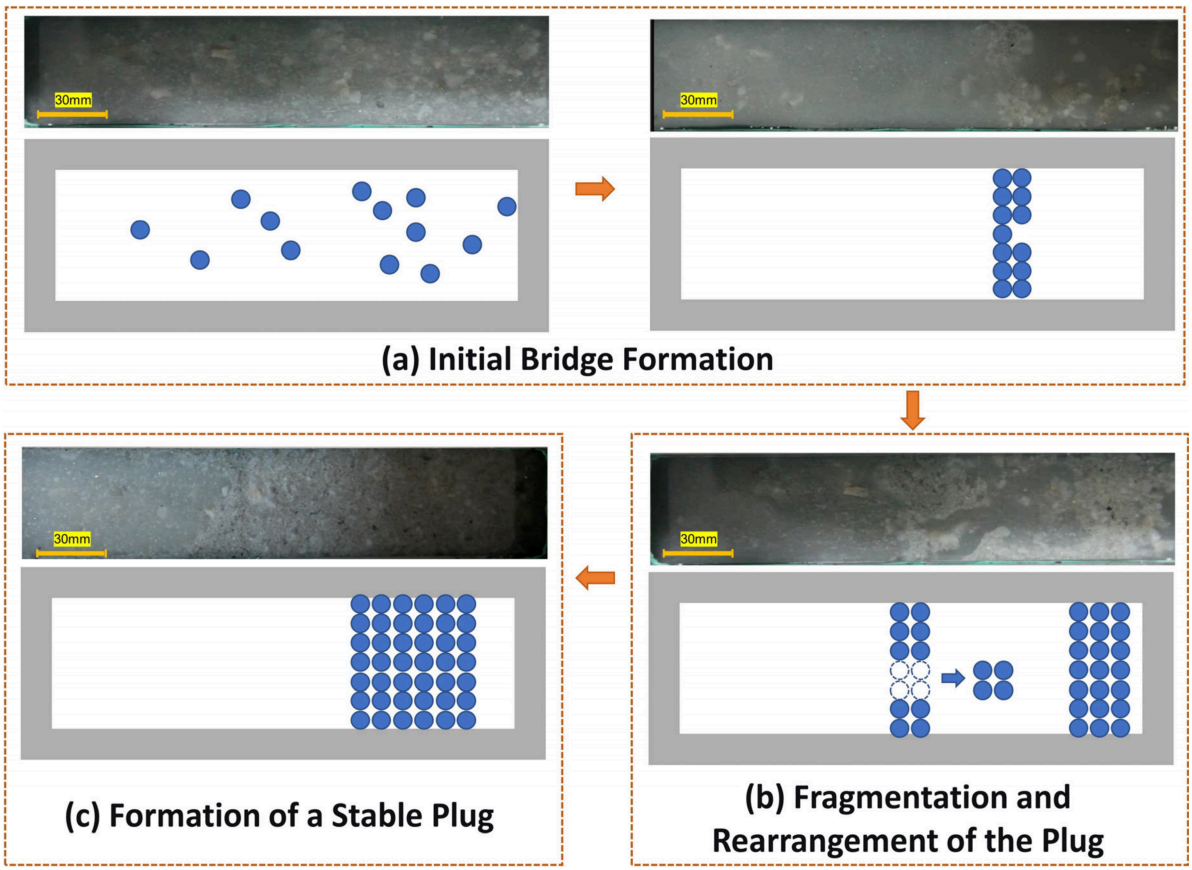


Figure 6. Schematic illustration of the plug formation process in the visual fracture model: (**a**) initial bridge formation, (**b**) fragmentation and reorganization of the plug, and (**c**) formation of a stable plug.

3.3.2. Influence of Fracture Width Coefficient on Plugging Effectiveness

The experimental results and corresponding plugging morphologies are presented in Figures 7–9. Analysis of the pressure-bearing curves in Figure 7 shows that the LCM formulation designed using the 0.6 W D_{90} rule failed to achieve effective plugging. During most of the experiment, the pressure remained at a relatively low level. At approximately 2400 s, the pressure briefly reached a maximum value of 6.7 MPa before rapidly dropping due to severe plugging-material loss. Afterward, the pressure could not be rebuilt, indicating plugging failure.

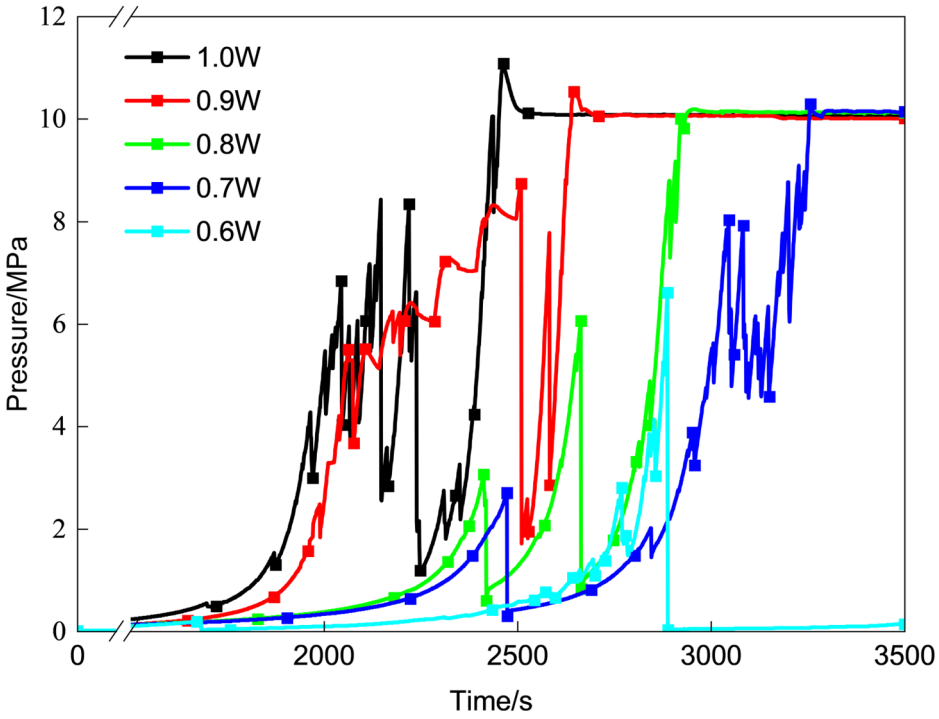


Figure 7. Pressure-bearing curves of plugging experiments under different fracture width factors based on the D_{90} rule (5–3 mm fracture model, 20% slurry concentration, target pressure of 10 MPa).

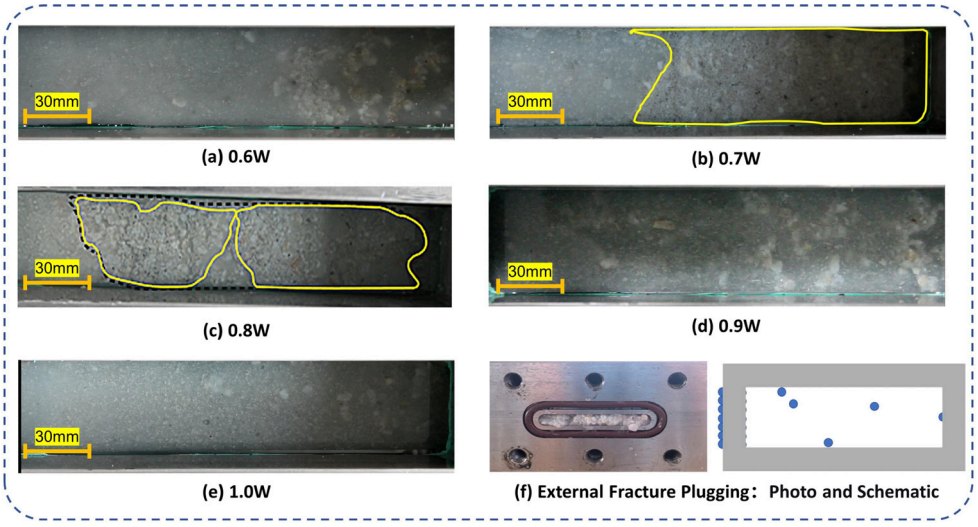


Figure 8. Final morphology of the plugging zones under different fracture width factors based on the D_{90} rule (5–3 mm fracture model, 20% slurry concentration, target pressure of 10 MPa).

In contrast, the 1.0 W formulation reached the target pressure of 10 MPa within approximately 1600 s, which was about 30% faster than the 0.8 W formulation. Based solely on the pressure-bearing curves, the 1.0 W formulation would therefore appear to provide superior plugging efficiency. However, visual observations shown in Figure 8 clearly demonstrated that neither the 0.9 W nor the 1.0 W experimental groups formed effective sealing structures inside the fracture (Figure 8d,e). Instead, plugging materials accumulated near the fracture entrance, resulting in "external plugging" (Figure 8f), where the fracture inlet was prematurely sealed and prevented drilling fluid from entering the fracture interior. This phenomenon produced an apparently favorable rapid pressure response despite the absence of effective internal plugging, as schematically illustrated in Figure 9.

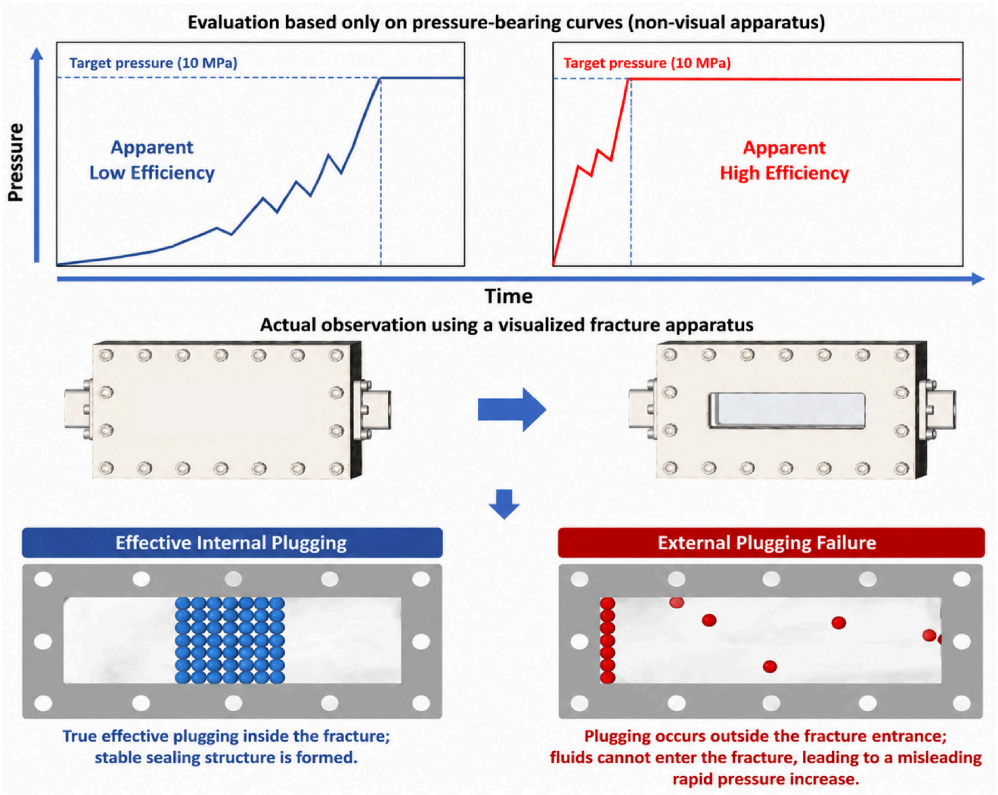


Figure 9. Schematic illustration of effective internal plugging and external plugging. External plugging may generate a rapid pressure increase despite the absence of effective sealing within the fracture.

By comparison, although the 0.8 W formulation required a longer time to reach the target pressure than the 0.9 W and 1.0 W formulations, it successfully formed a stable plugging structure within the fracture. Considering both the pressure-bearing curves and the visual observations, the 0.8 W D_{90} formulation exhibited the best overall plugging performance under the present experimental conditions. Therefore, the selection of 0.8 W as the optimized fracture-width coefficient was not based solely on the time required to reach the target pressure, but on the combined evaluation of pressure-bearing behavior, plugging location, and internal plugging stability. To further evaluate the repeatability of the plugging performance, the key plugging indicators obtained from repeated experiments are summarized in Table 4.

Table 4. Repeatability statistics of plugging experiments under different fracture width factors.

W Value	n	Time to 10 MPa/s	Maximum Pressure/MPa	Plugging Classification
0.6 W	3	—	6.17 ± 1.40	Plugging failure
0.7 W	3	3181 ± 102	10.0	Effective internal plugging
0.8 W	3	2942 ± 159	10.0	Effective internal plugging
0.9 W	3	2713 ± 176	10.0	Ineffective external plugging
1.0 W	3	2368 ± 176	10.0	Ineffective external plugging

The observed plugging behavior is closely related to the plug-formation mechanism described in Section 3.3.1. For the 0.9 W and 1.0 W formulations, the overall particle

size and maximum particle size were excessively large, making it difficult for particles to enter the fracture during the particle-entry and retention stage. Consequently, particles rapidly accumulated near the fracture entrance and formed premature bridging structures, eventually causing external plugging. In contrast, particles in the 0.6 W formulation could easily enter the fracture but were difficult to retain effectively because of their relatively small size. Most particles were carried out of the fracture by the fluid flow, while the few retained particles mainly relied on weak two-particle or multi-particle bridging structures, whose strength has been reported to be significantly lower than that of single-particle bridging structures [16,28]. As a result, the formed plugging structure was loose and unstable, with a maximum pressure-bearing capacity of only 6.7 MPa.

The visual observations further revealed that plugging effectiveness cannot be reliably evaluated solely based on pressure-bearing curves. Under certain experimental conditions, plugging materials may rapidly accumulate near the fracture inlet and generate a rapid pressure increase without forming an effective sealing structure inside the fracture. In contrast, effective plugging requires the formation of a stable plugging structure within the fracture interior.

Based on the coupled analysis of pressure-bearing response, plugging location, and structural stability observed in the visual fracture model, the plugging behaviors observed in this study can be categorized into three types: effective internal plugging, ineffective external plugging, and plugging failure. Effective internal plugging refers to the formation of a stable plugging structure inside the fracture, accompanied by stable pressure-bearing behavior. Ineffective external plugging refers to premature plugging near the fracture inlet without effective internal sealing, although rapid pressure buildup may still be observed. Plugging failure refers to the inability to establish or maintain a stable plugging structure under the target pressure conditions. The main characteristics of the different plugging classifications observed in the visual experiments are summarized in Table 5.

Table 5. Classification of plugging behaviors observed in the visual experiments.

Plugging Classification	Main Characteristics	Plugging Effectiveness
Effective internal plugging	Stable plugging structure formed inside the fracture	Effective
Ineffective external plugging	Premature plugging near the fracture inlet without effective internal sealing	Ineffective
Plugging failure	No stable plugging structure formed under target pressure conditions	Failed

These experiments further revealed an important limitation of conventional non-visual plugging evaluation methods based solely on pressure-bearing curves and fluid-loss data. Such methods may fail to distinguish effective internal plugging from external plugging, potentially leading to an overestimation of the actual plugging effectiveness.

3.3.3. Influence of Concentration on Plugging Effectiveness

The pressure-bearing curves presented in Figure 10 demonstrate that slurry concentration significantly affects plugging performance. In the 10% concentration group, pressure could not be effectively established throughout the experiment, indicating that the particle concentration was too low to provide sufficient particle participation for stable bridge formation within the fracture.

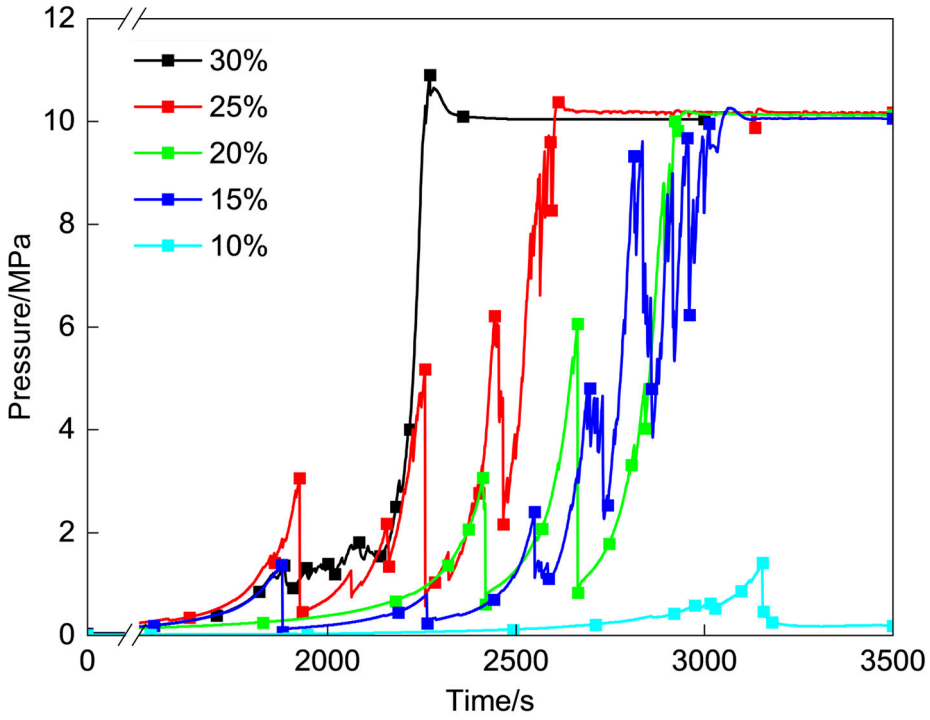


Figure 10. Pressure-bearing curves and plugging results under different slurry concentrations (5–3 mm fracture model, W = 0.8, target pressure of 10 MPa).

When the concentration increased to 15% and above, effective plugging was achieved in all experimental groups. Moreover, the time required to reach the target pressure of 10 MPa gradually decreased with increasing concentration. Specifically, the 15% concentration group required approximately 3100 s to reach the target pressure, while the 20% and 25% groups required approximately 2900 s and 2650 s, respectively. These results indicate that increasing slurry concentration within an appropriate range can enhance particle collision probability and accelerate bridge formation, thereby improving plugging efficiency. The repeatability statistics of the key plugging indicators under different slurry concentrations are summarized in Table 6.

Table 6. Repeatability statistics of plugging experiments under different slurry concentrations.

Concentration/%	n	Time to 10 MPa/s	Maximum Pressure/MPa	Plugging Classification
10	3	—	2.11 ± 0.32	Plugging failure
15	3	3178 ± 125	10.0	Effective internal plugging
20	3	2999 ± 76	10.0	Effective internal plugging
25	3	2581 ± 75	10.0	Effective internal plugging
30	3	2149 ± 102	10.0	Ineffective external plugging

However, the 30% concentration group reached the pressure peak within approximately 2250 s, which was significantly faster than the other groups. Combined with video observations and post-experiment disassembly results, a typical case of "external plugging" was identified in this group. Large quantities of particles rapidly accumulated near the fracture entrance and prematurely sealed the inlet before entering the fracture interior to form an effective internal plugging structure. As a result, the pressure-bearing curve exhibited an apparently rapid pressure increase despite the absence of effective fracture sealing.

These observations indicate that continuously increasing slurry concentration does not necessarily improve plugging performance. Once the concentration exceeds a certain threshold, the number of particles entering the fracture entrance per unit time increases sharply, resulting in severe particle crowding and interference near the inlet region. This significantly increases the probability of premature particle bridging and external plugging during the particle-entry and retention stage.

Although such entrance plugging can rapidly block fluid flow and produce an apparently favorable pressure response, the resulting structure is weak and unstable because the fracture channel itself is not effectively sealed. In practical field operations, such misleading pressure signals may lead to repeated leakage after re-pressurization, representing a typical case of ineffective plugging.

3.3.4. Plugging Effectiveness in Fractures with Different Widths

The pressure-bearing curves shown in Figure 11 indicate that the plugging formulations designed using the same D_{90} rule exhibited a high degree of consistency under different fracture-width conditions. The overall shapes of the three pressure-bearing curves were similar and all displayed a stepwise increasing trend. For the 3–1 mm fracture, approximately 2550 s was required to reach and stabilize at 10 MPa, while an additional 210 s was required to increase from 10 MPa to 15 MPa. For the 5–3 mm fracture, approximately 2520 s was required to reach 10 MPa, and approximately 90 s was required to increase from 10 MPa to 15 MPa. The 8–5 mm fracture required the longest time to reach 10 MPa, approximately 2650 s, while approximately 130 s was required to increase from 10 MPa to 15 MPa. Under the present experimental conditions, the maximum difference in the time required to reach the same pressure threshold among the different fracture-width models was within 7%, indicating that the optimized plugging formulation exhibited good scale adaptability across different fracture sizes.

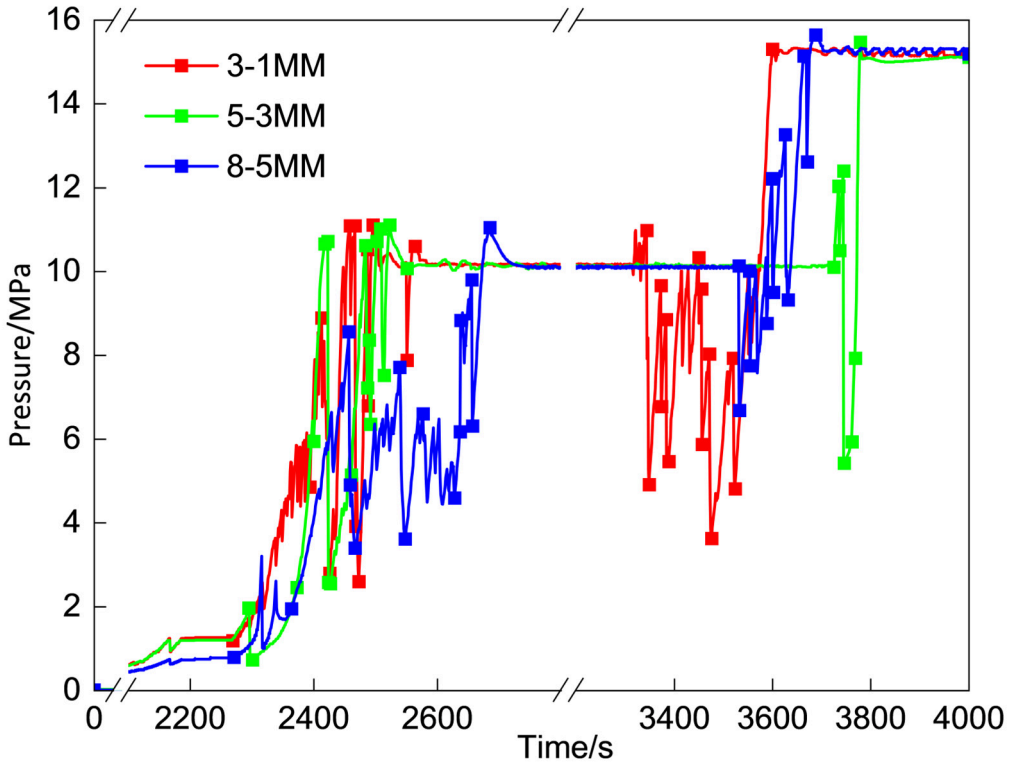


Figure 11. Pressure-bearing curves of plugging experiments under different fracture-width profiles (3–1 mm, 5–3 mm, and 8–5 mm fracture models, W = 0.8, slurry concentration of 25%, target pressure of 15 MPa).

The post-experiment plugging morphologies shown in Figure 12 further confirmed this behavior. In all three fracture models, the plugging zones were located in the middle-to-rear sections of the fractures, occupying approximately one-half to two-thirds of the total fracture length. The plugging structures were relatively dense and exhibited similar spatial distributions.

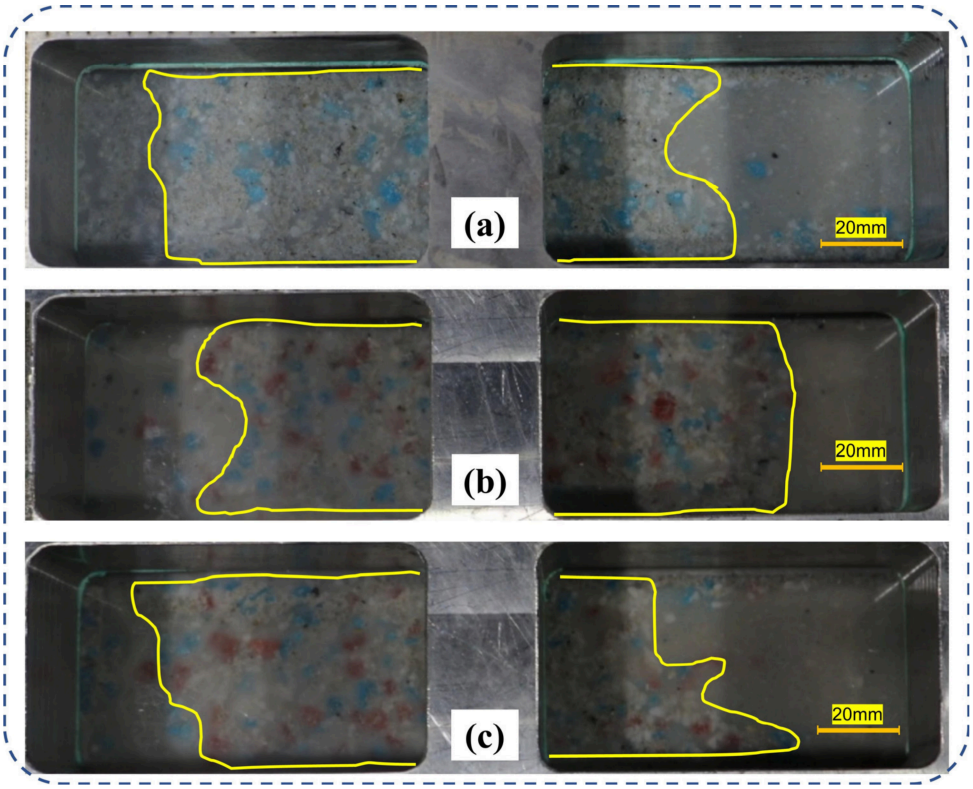


Figure 12. Final morphology of the plugs formed in different fracture-width profiles: (**a**) 3–1 mm, (**b**) 5–3 mm, and (**c**) 8–5 mm fracture models (W = 0.8, slurry concentration of 25%, target pressure of 15 MPa).

Mechanistically, this cross-scale consistency verifies the scaling principle of the D_{90} rule. Because the formulations were designed based on a constant fracture-width coefficient (W), meaning that the characteristic particle size D_{90} maintained a fixed proportional relationship with the fracture width, the relative geometric relationship between the particles and the fracture remained similar across different fracture scales. This geometric similarity resulted in comparable particle transport trajectories, collision probabilities, and bridging locations within the fractures, thereby producing similar plug-formation processes under different fracture-width conditions.

Furthermore, the pressure-bearing process shown in Figure 11 was conducted in two pressure-buildup stages. The target pressure was first set to 10 MPa. After the pressure reached 10 MPa and was maintained for a period of time, the target pressure was further increased to 15 MPa. Therefore, the pressure-holding period at 10 MPa was not included in the analysis of pressure fluctuation events.

During the two pressure-buildup stages, the pressure-bearing curves exhibited several distinct pressure-drop and pressure-recovery events before reaching a stable pressure-bearing state. In the visual observations, pressure drops greater than 1 MPa generally coincided with visible fragmentation and reorganization of the plugging structure. In contrast, smaller pressure oscillations were difficult to distinguish from fluctuations caused by pump regulation, pressure-control adjustment, or minor structural disturbance of the

plugging zone. Therefore, a pressure-drop amplitude of 1 MPa was used as the threshold for identifying major pressure fluctuation events. Based on this criterion, the number of major pressure fluctuation events (N) and the maximum pressure-drop amplitude (ΔPmax) were extracted from the pressure-bearing curves, as summarized in Table 7.

Table 7. Quantitative characteristics of major pressure fluctuations during staged pressure buildup.

Fracture-Width Profile	N Before 10 MPa	ΔPmax Before 10 MPa/MPa	N from 10 to 15 MPa	ΔPmax from 10 to 15 MPa/MPa
3–1 mm	12	6.82	10	5.49
5–3 mm	5	7.73	2	6.10
8–5 mm	6	4.01	7	2.93

Note: The pressure-holding period at 10 MPa was excluded from the fluctuation statistics. A major pressure fluctuation event was identified when the pressure-drop amplitude exceeded 1 MPa and was followed by pressure recovery.

The quantified pressure fluctuation characteristics show that the pressure buildup process was accompanied by repeated pressure-drop and pressure-recovery events. For the 3–1 mm fracture, 12 major pressure fluctuation events were identified before 10 MPa, with a maximum pressure-drop amplitude of 6.82 MPa; during the 10–15 MPa stage, 10 events were identified, with a maximum pressure-drop amplitude of 5.49 MPa. For the 5–3 mm fracture, 5 and 2 major pressure fluctuation events were identified in the two pressure-buildup stages, with maximum pressure-drop amplitudes of 7.73 MPa and 6.10 MPa, respectively. For the 8–5 mm fracture, 6 and 7 major pressure fluctuation events were identified, with maximum pressure-drop amplitudes of 4.01 MPa and 2.93 MPa, respectively. These results indicate that the formation of stable internal plugging structures was accompanied by repeated fragmentation and reorganization processes.

The pressure-drop segments corresponded to the fragmentation stage of the plugging structure, whereas the subsequent pressure-recovery segments corresponded to the reorganization and re-establishment of the plugging structure. This pressure-response pattern is consistent with the plug-formation process shown in Figure 6 and explains the stepwise increase in pressure observed in Figure 11.

These adaptability tests provide a preliminary verification of the scale adaptability of the optimized 0.8 W coefficient within the tested fracture-width range. Because the D_{90} value was scaled according to the corresponding fracture width, the relative particle-to-fracture size relationship was maintained across different fracture models. Therefore, similar plugging processes and stable internal plugging morphologies were obtained under different fracture-width profiles. However, the 0.8 W coefficient should not be regarded as a universal constant, and its applicability to other LCM systems, fracture roughness conditions, temperature/stress environments, and field-scale fracture networks requires further verification.

3.3.5. Limitations and Scope

In this study, the experimental model employs smooth borosilicate fracture surfaces and a controlled wedge height. Although the apparatus has a maximum simulated temperature capability of 160 °C, the present experiments were conducted under room-temperature conditions and therefore did not systematically examine the effects of temperature-dependent slurry properties on LCM transport, retention, and plugging stability. In addition, the current setup cannot fully reproduce the true roughness evolution of deep natural fractures or their in situ triaxial stress state. Previous studies on particle-containing fluids have shown that thermophysical properties and flow parameters, such as viscosity, inlet temperature, dispersed-phase volume fraction, and flow rate, can affect transport behavior in heterogeneous porous media [29].

These simplified conditions may influence the experimental results in several ways. First, the use of smooth borosilicate fracture surfaces may reduce wall friction and mechanical interlocking between LCM particles and the fracture wall compared with rough natural fractures. When fracture roughness helps trap particles inside the fracture, the smooth-wall model may make particles easier to transport or wash out, and therefore may underestimate particle retention and plug stability. However, rough natural fractures may also generate local aperture heterogeneity and preferential flow paths, which can promote particle accumulation near the fracture inlet and increase the probability of premature external plugging. Therefore, the influence of fracture roughness is not unidirectional: it may enhance internal plug stability in some cases, but may also intensify localized entrance plugging depending on the roughness morphology and flow-path distribution.

Second, room-temperature testing may overestimate slurry suspension stability under high-temperature downhole conditions. Elevated temperature can alter slurry viscosity and particle-settling behavior, thereby affecting LCM transport, retention, and the formation rate of the plugging zone. In particular, reduced viscosity at elevated temperature may weaken particle suspension and promote faster particle settling or local particle enrichment, which could increase the risk of non-uniform plugging or premature external plugging. Therefore, the present room-temperature results should be interpreted as a controlled baseline rather than a complete representation of high-temperature field behavior.

Third, the absence of in situ triaxial stress means that fracture aperture variation, stress-induced closure, and roughness-contact evolution were not reproduced. Under field stress conditions, fracture closure may reduce the effective aperture and increase the relative particle-to-fracture size ratio. This may shift the optimal D_{90} coefficient toward a lower value and increase the possibility of entrance bridging. Conversely, pressure-induced fracture dilation may require larger particles or higher slurry concentration to maintain effective plugging. Therefore, the fixed-aperture wedge model may underestimate the influence of dynamic fracture deformation on the balance between effective internal plugging and premature external plugging.

Overall, these simplified conditions may affect the absolute plugging time, pressure-bearing response, and critical coefficient range. However, they do not change the central conclusion that non-visual pressure-based evaluation alone may misidentify external plugging as effective plugging. Future research incorporating rough fracture surfaces, temperature-controlled slurry tests, and coupled stress conditions could further quantify how fracture roughness, slurry rheology, thermal effects, and stress-induced aperture variation influence the critical balance between effective internal plugging and premature external plugging, thereby enhancing the direct field applicability of the findings.

4. Field Application

Well BD-X, located on the eastern flank of a local high in the Dabei-12 structure, is a five-section appraisal well with a designed depth of 6290 m, targeting the Cretaceous Baxigai Formation (Figure 13). During drilling of the fourth section through the salt-gypsum interval of the Kumugeliemu Group, eight lost-circulation incidents occurred. The maximum loss rate reached 100 m^3/h, resulting in total fluid loss at the wellhead. The cumulative drilling-fluid loss reached 202.7 m^3, causing 141 h of non-productive time.

A total-loss incident occurred at a depth of 6043 m while drilling the fourth section. The initial field treatment involved pumping 25 m^3 of a high-concentration LCM slurry with a drilling-fluid density of 1.85 g/cm^3, followed by 2 h of static settling. The plugging formulation consisted of 65% JXD-4 and 5% JXD-3, with a total concentration of 70%. However, circulation loss reoccurred immediately after pumping was resumed.

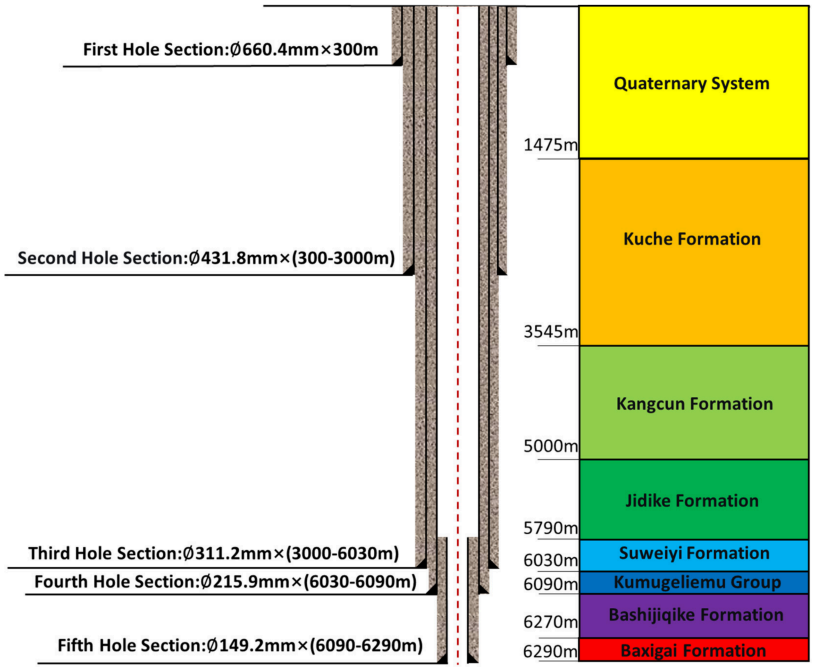


Figure 13. Wellbore Profile and Formation Chart for Well BD-X.

Based on the laboratory findings of this study, this failure was interpreted as a typical case of premature external plugging. The excessively high concentration and coarse particle composition likely caused rapid particle accumulation near the fracture entrance, forming an unstable external plugging structure that was displaced once circulation resumed. To improve the field applicability of the laboratory findings, the fracture width of the lost-circulation interval was estimated using the LC-Plugging fracture inversion software developed in the Tarim Oilfield. The estimated fracture width was approximately 3.12 mm, which corresponded well to the 3–1 mm fracture-width profile investigated in the laboratory experiments. Based on the estimated fracture width and the plugging optimization strategy obtained from the visual plugging experiments, the field plugging formulation was subsequently redesigned.

Guided by the laboratory results, the field formulation was subsequently optimized to a graded LCM system consisting of 8% JXD-4, 10% JXD-3, and 7% JXD-2, with a total concentration of 25%. A total of 10 m^3 of the optimized slurry with a drilling-fluid density of 1.85 g/cm^3 was pumped into the lost-circulation interval. After treatment, the drill string was pulled out to 3700 m, during which the fluid level remained normal and no further losses were observed, confirming successful plugging without recurrence.

While drilling the fifth section into the Cretaceous Bashijiqike Formation at a depth of 6228 m, which is characterized by developed fractures and microfractures, the well again experienced minor lost circulation at a rate of 4.8 m^3/h. The fracture width of this interval was estimated to be approximately 2.87 mm using the same fracture inversion method, which also fell within the fracture-width range investigated in the laboratory experiments. Based on the laboratory findings and field operational experience, a tailored LCM formulation was designed using available JXD-series materials and SQD-98 (Fine), consisting of 6% JXD-4, 9% JXD-3, 5% JXD-2, and 4% SQD-98 (Fine), with a total concentration of 24%.

A total of 20 m^3 of this slurry, with a drilling-fluid density of 1.91 g/cm^3, was pumped for lost-circulation control while drilling. Following treatment, the loss rate decreased from 4.8 m^3/h to zero, and no recurrence was observed during subsequent operations.

The detailed field treatment procedures, operational parameters, and plugging results are summarized in Table 8. The field applications demonstrate that the optimized LCM

formulations developed based on the visual plugging experiments can effectively improve plugging stability and reduce the risk of recurrence associated with premature external plugging. The field results further indicate that the visual-pressure coupled evaluation approach proposed in this study is particularly applicable to fractured formations with severe or repeated lost circulation, where stable internal plugging structures are required to maintain long-term plugging effectiveness. Under such conditions, optimization of LCM grading and concentration is critical for improving plugging durability. However, the optimized formulations and operational parameters proposed in this study were developed under the current drilling-fluid system and field leakage conditions. Their applicability to other formation types, drilling-fluid systems, and complex fracture-network conditions still requires further engineering verification.

Table 8. Field plugging treatments, operational parameters, and results for Well BD-X.

Well Depth	Estimated Fracture Width	Type	Formulation	Total Concentration	Operational Parameters	Result
6043 m	3.12 mm	Initial treatment	65%JXD-4 + 5%JXD-3	70%	25 m^3 slurry; mud density: 1.85 g/cm^3; pumping followed by 2 h static settling	Total loss recurred after resuming circulation
		Optimized treatment	8%JXD-4 + 10%JXD-3 + 7%JXD-2	25%	10 m^3 slurry; mud density: 1.85 g/cm^3; optimized graded LCM treatment	Successful plugging, with no recurrence after resuming circulation
6228 m	2.87 mm	Leveraging Field Experience and Research Theory	6%JXD-4 + 9%JXD-3 + 5%JXD-2 + 4%SQD-98 (fine)	24%	20 m^3 slurry; mud density: 1.91 g/cm^3; lost-circulation control while drilling	Minor loss (4.8 m^3/h) reduced to zero, with no recurrence

5. Conclusions

(1) A visual experimental apparatus with high pressure-bearing capacity and large-window observation capability was successfully developed for investigating the plugging process in fractured formations. Compared with conventional visual devices, the apparatus enables direct observation of particle transport, retention, bridge formation, and plug evolution under higher pressure conditions, thereby providing a more reliable experimental platform for evaluating plugging effectiveness and investigating plugging mechanisms.

(2) The visual experiments demonstrated that plugging effectiveness cannot be reliably evaluated solely based on pressure-bearing curves and fluid-loss data. Excessively large fracture-width coefficients or excessively high slurry concentrations can lead to premature ineffective external plugging, in which plugging materials accumulate near the fracture entrance without forming an effective internal plugging structure. Although such cases may exhibit rapid pressure buildup, visual observations confirmed that the fracture itself remained insufficiently sealed. This finding provides a mechanistic explanation for the field problem of repeated loss recurrence after circulation restart.

(3) Under the present experimental conditions, the optimized LCM formulation designed based on the Ideal Packing Theory and the D_{90} rule, with a fracture-width coefficient of 0.8 W and a slurry concentration of 25%, exhibited the best overall plugging performance. The optimized formulation successfully formed stable internal plugging structures under different fracture-width conditions and demonstrated good scale adaptability.

(4) The proposed plugging design method and optimized LCM formulations were further validated through field applications in Well BD-X. The optimized graded LCM treatments successfully controlled both severe total-loss and minor-loss conditions without recurrence, demonstrating that the laboratory findings possess practical applicability and effectiveness under real drilling conditions.

Author Contributions: Conceptualization, Y.Y., X.L., F.G., N.Y. and S.D.; Methodology, X.L., F.G., N.Y., F.L. and Y.G.; Software, X.L.; Investigation, N.Y., F.L., Y.G. and S.D.; Writing—original draft, X.L. and F.G.; Writing—review & editing, X.L.; Visualization, X.L. and F.G.; Supervision, Y.Y.; Project administration, Y.Y.; Funding acquisition, Y.Y. All authors have read and agreed to the published version of the manuscript.

Funding: This study received support and funding from the National Natural Science Foundation of China (No. 52074321).

Data Availability Statement: The original contributions presented in this study are included in the article. Further inquiries can be directed to the corresponding author.

Conflicts of Interest: Author Fuliang Guo were employed by the Tarim Oilfield Company. The remaining authors declare that the research was conducted in the absence of any commercial or financial relationships that could be construed as a potential conflict of interest.

References

1. Kang, Y.; Xu, C.; Tang, L.; Li, S.; Li, D. Constructing a tough shield around the wellbore: Theory and method for lost-circulation control. *Pet. Explor. Dev.* **2014**, *41*, 520–527. [CrossRef]
2. Xu, C.; Yan, X.; Kang, Y.; You, L.; Zhang, J. Structural failure mechanism and strengthening method of fracture plugging zone for lost circulation control in deep naturally fractured reservoirs. *Pet. Explor. Dev.* **2020**, *47*, 430–440. [CrossRef]
3. Sun, J.; Bai, Y.; Cheng, R.; Lyu, K.; Liu, F.; Feng, J.; Lei, S.; Zhang, J.; Hao, H. Research progress and prospect of plugging technologies for fractured formation with severe lost circulation. *Pet. Explor. Dev.* **2021**, *48*, 630–638. [CrossRef]
4. Lv, K.; Wang, C.; Lei, S.; Sun, J.; Bai, Y.; Wang, J.; Wang, R.; Wang, J. Dynamic behavior and mitigation methods for drilling fluid loss in fractured formations. *J. China Univ. Pet. (Ed. Nat. Sci.)* **2022**, *46*, 85–93.
5. Chen, G.; He, Y.; Qiu, Z.; Guan, J.; Wang, X. Research and application for the fine identification method of lost circulation characteristics during drilling. *Pet. Drill. Tech.* **2024**, *52*, 26–31.
6. Xu, T.; Shen, W.; Feng, J.; Liu, J.; Miao, H. *Drilling Engineering Leakage Prevention and Plugging Technology*, 2nd ed.; Petroleum Industry Press: Beijing, China, 2021.
7. Hettama, M.; Horsrud, P.; Taugbol, K.; Friedheim, J.; Huynh, H.; Sanders, M.W.; Young, S. Development of an innovative high-pressure testing device for the evaluation of drilling fluid systems and drilling fluid additives within fractured permeable zones. In *Proceedings of the Offshore Mediterranean Conference and Exhibition, Ravenna, Italy, 28 March 2007*; OnePetro: Richardson, TX, USA, 2007.
8. Deng, Z. Design of an Evaluation Device for Leak Plugging and Study on the Efficacy Evaluation of Working Fluids. Master's Thesis, Southwest Petroleum University, Chengdu, China, 2012.
9. Dou, B.; Shu, S.; Guo, J.; Li, X.; Liu, W. Test device of hi-fi simulation thief for leakage plugging evaluation. *China Pet. Mach.* **2009**, *37*, 5–7+89.
10. China University of Petroleum, Beijing. Stress-Sensitive Formation Drilling Leakage Plugging Simulation and Evaluation Device. CN201020626023.0, 20 July 2011.
11. Southwest Petroleum University. A Leak Plugging Device Considering the Dynamic Change of Fracture Width. 201820537818.0, 2 November 2018.
12. Jiang, Z.; Meng, H.; Xiong, C.; Xie, Z. Design of a lost circulation control test device simulating annular flow. *China Pet. Mach.* **2019**, *47*, 44–49.
13. Ma, C.; Dou, Y.; Deng, J.; Feng, Y.; Ai, E.; Zhao, K.; Hui, C. Development and application of dynamic fracture plugging test device. *China Pet. Mach.* **2023**, *51*, 25–30.
14. Zhao, Z.; Pu, X.; Wang, G.; Huang, S.; Xiang, C.; Yang, Z. Study on drilling fluid bridge plugging technology for fractured formation. *Drill. Fluid Complet. Fluid* **2012**, *29*, 44–46+94–95.
15. Southwest Petroleum University. A Plugging Test Device for Simulating Smooth and Rough Fracture Walls. 201520890759.1, 6 April 2016.

16. China University of Petroleum, Beijing. True Triaxial Drilling Leakage Plugging Simulation and Evaluation Device. CN201020104973.7, 10 November 2010.
17. Wang, T.; Ye, Y.; Zhu, J.; Zhang, Z.; Lu, H.; Li, C.; Sun, Z. Research on a new method for simulation of fractured plugging based on 3D scanning and printing technology. *Drill. Fluid Complet. Fluid* **2023**, *40*, 571–577.
18. Shi, B.; Hu, X.; Gao, S.; Xu, J.; Lin, Y. Visualization sealing simulation test and evaluation of hard brittle shale microfracture. *Pet. Drill. Tech.* **2014**, *42*, 32–37.
19. Huang, H.; Babadagli, T.; Li, H.; Develi, K.; Zhou, D. A visual experimental study on proppants transport in rough vertical fractures. *Int. J. Rock Mech. Min. Sci.* **2020**, *134*, 104446. [CrossRef]
20. Li, Z. Research on Gas-Liquid Displacement in Vertical Crack and Drilling Fluid Plugging Technology to Prevent Gas Cut. Ph.D. Thesis, Petroleum University, Chengdu, China, 2014.
21. Xu, C.; Zhang, H.; Kang, Y.; Zhang, J.; Bai, Y.; Zhang, J.; You, Z. Physical plugging of lost circulation fractures at microscopic level. *Fuel* **2022**, *317*, 123477. [CrossRef]
22. Guo, J.; Zhan, L.; Lu, Q.; Qi, T.; Liu, Y.; Wang, X.; Chen, C.; Gou, X. Plugging behaviors of temporary plugging particles in hydraulic fractures. *Pet. Explor. Dev.* **2023**, *50*, 409–415. [CrossRef]
23. Zhang, J.; Yan, J. New theory and method for optimizing the particle size distribution for bridging agent in drilling fluid. *Acta Pet. Sin.* **2004**, *25*, 88–91+95.
24. You, L.; Tan, Q.; Kang, Y.; Zhang, X.; Xu, C.; Lin, C. Optimizing the particle size distribution of drill-in fluids based on fractal characteristics of porous media and solid particles. *J. Pet. Sci. Eng.* **2019**, *171*, 1223–1231. [CrossRef]
25. Liu, Y.; Zhang, P.; Zheng, X.; Huang, J.; Wei, S.; Chen, Q.; Ma, T. Experimental study on the updated selection criterion for particle size distribution of lost circulation materials. *Geomech. Geophys. Geo-Energy Geo-Resour.* **2026**, *12*, 28. [CrossRef]
26. Li, B.; Feng, Y.; Ma, C.; Li, S.; Lai, C.; Zhang, S.; Su, F. Particle size optimization of lost circulation materials: A comprehensive experimental study. In Proceedings of the 57th U.S. Rock Mechanics/Geomechanics Symposium, Atlanta, GA, USA, 25–28 June 2023. ARMA-2023-0359.
27. Yang, C.; Ye, Y.; Wang, R.; Tian, M.; Zou, S.; Liu, D.; Wang, S.; Guo, F. The application of CT scanning in visual plugging evaluation. In Proceedings of the 2025 International Conference on Electrical Drives, Power Electronics and Engineering (EDPEE), Athens, Greece, 26–28 March 2025; pp. 95–101.
28. Sacramento, R.N.; Yang, Y.; You, Z.; Waldmann, A.; Martins, A.L.; Vaz, A.S.L.; Zitha, P.L.J.; Bedrikovetsky, P. Deep bed and cake filtration of two-size particle suspension in porous media. *J. Pet. Sci. Eng.* **2015**, *126*, 201–210. [CrossRef]
29. Al-Yaari, A.; Ching, D.L.C.; Sakidin, H.; Muthuvalu, M.S.; Zafar, M.; Haruna, A.; Merican, Z.M.A.; Yunus, R.B.; Al-Dhawi, B.N.S.; Jagaba, A.H. The effects of nanofluid thermophysical properties on enhanced oil recovery in a heterogeneous porous media. *Case Stud. Chem. Environ. Eng.* **2024**, *9*, 100556.

Disclaimer/Publisher's Note: The statements, opinions and data contained in all publications are solely those of the individual author(s) and contributor(s) and not of MDPI and/or the editor(s). MDPI and/or the editor(s) disclaim responsibility for any injury to people or property resulting from any ideas, methods, instructions or products referred to in the content.